

Research Article

SIMMER-III Analyses of Local Fuel-Coolant Interactions in a Simulated Molten Fuel Pool: Effect of Coolant Quantity

Songbai Cheng,¹ Ken-ichi Matsuba,¹ Mikio Isozaki,¹ Kenji Kamiyama,¹ Tohru Suzuki,¹ and Yoshiharu Tobita²

¹Advanced Fast Reactor Cycle System Research and Development Center, Japan Atomic Energy Agency, 4002 Narita, Oarai, Ibaraki 311-1393, Japan

²Monju Project Management and Engineering Center, Japan Atomic Energy Agency, 1 Shiraki, Tsuruga, Fukui 919-1279, Japan

Correspondence should be addressed to Songbai Cheng; cheng.songbai@jaea.go.jp

Received 7 August 2014; Revised 22 December 2014; Accepted 22 December 2014

Academic Editor: Borut Mavko

Copyright © 2015 Songbai Cheng et al. This is an open access article distributed under the Creative Commons Attribution License, which permits unrestricted use, distribution, and reproduction in any medium, provided the original work is properly cited.

Studies on local fuel-coolant interactions (FCI) in a molten pool are important for the analyses of severe accidents that could occur for sodium-cooled fast reactors (SFRs). To clarify the mechanisms underlying this interaction, in recent years, several experimental tests, with comparatively larger difference in coolant volumes, were conducted at the Japan Atomic Energy Agency by delivering a given quantity of water into a molten pool formed with a low-melting-point alloy. In this study, to further understand this interaction, interaction characteristics including the pressure buildup as well as mechanical energy release and its conversion efficiency are investigated using the SIMMER-III, an advanced fast reactor safety analysis code. It is found that the SIMMER-III code not only reasonably simulates the transient pressure and temperature variations during local FCIs, but also supports the limited tendency of pressurization and resultant mechanical energy release as observed from experiments when the volume of water delivered into the pool increases. The performed analyses also suggest that the most probable reason leading to such limited tendency should be primarily due to an isolation effect of vapor bubbles generated at the water-melt interface.

1. Introduction

The disaster in March 2011 at the Fukushima Daiichi Nuclear Power Plant in Japan has caused many people to realize that severe accidents might occur, even if their probability is extremely low [1–3]. For sodium-cooled fast reactors (SFR), since the core is not generally designed at the most reactive configurations, in the past, the sequences and consequences of hypothetical severe accidents have been extensively investigated [4–7]. It is believed that, by assuming pessimistic conditions (e.g., minimal fuel discharge from the core), the accident might proceed into a transition phase where a large whole-core scale pool containing sufficient fuel capable of exceeding the prompt criticality by fuel compaction can be formed (see Figure 1) [8, 9]. Since, during the pool enlargement, a certain amount of liquid coolant might be entrapped within the pool (e.g., due to the failure of control rod guide tube), local fuel-coolant interaction (FCI) in the

fuel pool is regarded as one of the various initiators that could lead to such compactive fluid motions [4].

Unfortunately, it is instructive to note that, over the past decades, although extensive studies (e.g., CCM [10], KROTOS [11], FARO [12], and TROI [13]), with an emphasis on ascertaining the mechanisms of steam explosion and debris bed formation in a FCI, have been conducted, most of them were performed in a fuel-injection (FI) mode, namely, by injecting or pouring melt into a coolant pool, while the knowledge and data gained from a coolant-injection (CI) mode has not been accumulated sufficiently, especially in a scenario where a certain amount of liquid coolant is entrapped within a larger melt pool. Park et al. [14] and Sibamoto et al. [15] are the few representative authors that independently performed their investigations in a CI mode within various situations (such as energetic or nonenergetic conditions). In their studies, valuable information and data on the jet penetration behavior (e.g., penetration velocity,

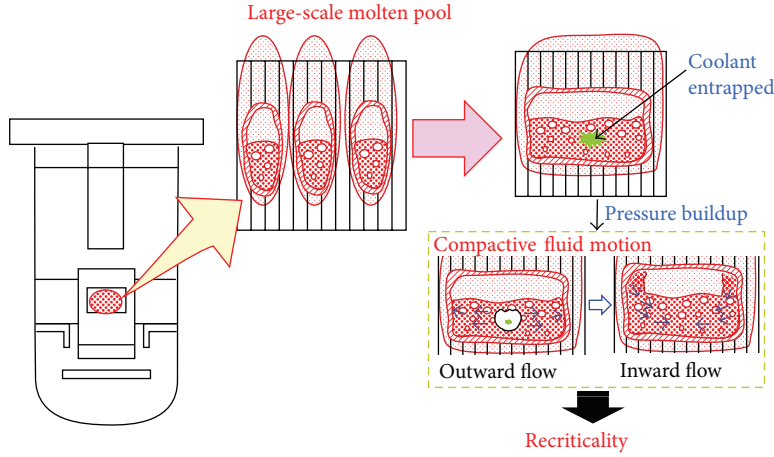


FIGURE 1: Large-scale molten pool formed during transition phase.

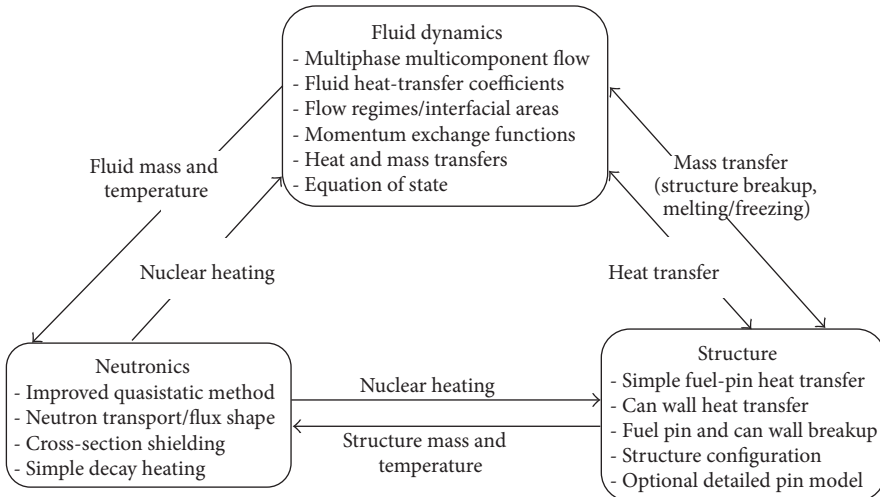


FIGURE 2: SIMMER-III overall code structure.

depth, and cavity characteristics) were collected, while the knowledge on the pressure buildup by local FCIs in the pool is still limited, despite their crucial importance for accident progression evaluation.

To clarify the characteristics of molten fuel pool at various disturbances, in the past years, several series of studies, including specifically designed in-pile and out-of-pile experiments as well as numerical simulations [7], have been initiated at the Japan Atomic Energy Agency (JAEA). Among those studies, for the local FCIs, as reported in a recent publication [16], several tests were conducted by delivering a given quantity of water into a molten pool formed with a low-melting-point alloy. From the experimental analyses [16], it was recognized that, for a given melt and water temperature within the nonfilm boiling range, with the increasing water volume, a limited pressure buildup is achievable for both the melt and cover gas regions. In this study, to further understand the mechanisms underlying this interaction, SIMMER-III, an advanced fast reactor safety analysis code [17–19], which is believed to be a unique simulation code currently in

the world for event progression analyses in a whole-core scale [7], is used for analyses. In Section 2, the physical models and methods of this code are concisely described with an emphasis on the main features related to FCI analysis, while, in Section 3, after a briefing of the performed experiments, the analytical geometry and conditions are determined. Finally, in Section 4, detailed interpretations and discussions on the obtained results (e.g., pressure buildup, mechanical energy release, and conversion efficiency) are further presented.

2. Models and Methods of SIMMER-III

SIMMER-III is a two-dimensional, multivelocity field, multiphase, multicomponent, Eulerian, fluid-dynamics code coupled with a structure (fuel-pin) model and a space- and energy-dependent neutron kinetics model (see Figure 2) [18]. The fluid-dynamics portion, which constitutes about two-thirds of the code, is interfaced with the structure model through heat and mass transfer at structure surfaces, while the neutronics portion provides nuclear heat sources based

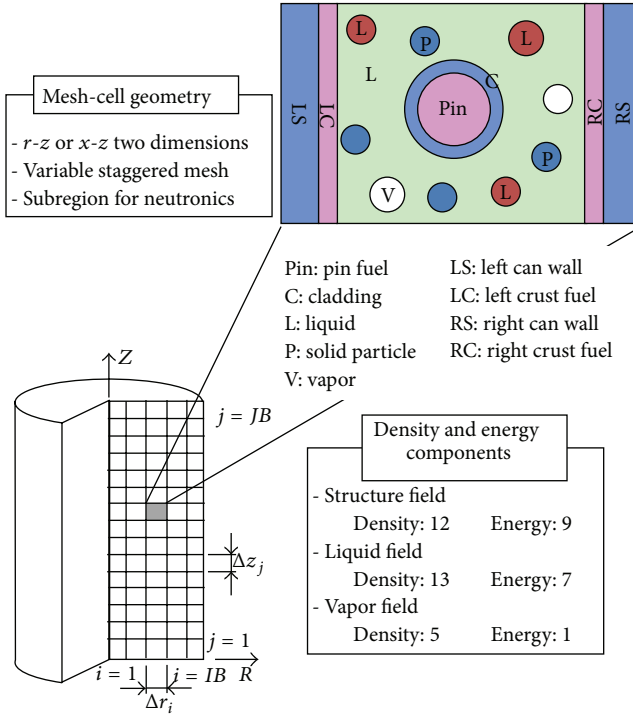


FIGURE 3: SIMMER-III geometric framework.

on the mass and energy distributions calculated by the other code elements [18, 19].

The basic geometric structure of SIMMER-III is a two-dimensional R - Z system (see Figure 3), although optionally an X - Z system can be also used for various fluid-dynamics calculations. The code models five basic SFR core materials: mixed-oxide fuel, stainless steel, sodium, control (B_4C), and fission gas. Since a material can exist at different physical states during core disruptive accidents (CDAs), fuel, for example, should be represented by fabricated pin fuel, liquid fuel, a refrozen crust on structure, solid particles, broken fuel pellets (also called chunks), and fuel vapor. As a result, as depicted in Figure 3, a total of 30 density components and 17 energy components are being modeled in the current code [19].

2.1. Fluid-Dynamics Model. In the SIMMER-III code, the following conservation equations involving fluid mass, momentum, and internal energy are solved:

$$\begin{aligned} \frac{\partial \bar{\rho}_m}{\partial t} + \nabla \cdot (\bar{\rho}_m \vec{v}_q) &= -\Gamma_M, \\ \frac{\partial \bar{\rho}_m \vec{v}_q}{\partial t} + \sum_{m \in q} \nabla \cdot (\bar{\rho}_m \vec{v}_q \vec{v}_q) + \alpha_q \nabla P & \\ - \bar{\rho}_q \vec{g} + K_{qs} \vec{v}_q - \sum_{q'} K_{qq'} (\vec{v}_{q'} - \vec{v}_q) - \overrightarrow{VM}_q & \\ = - \sum_{q'} \Gamma_{qq'} [H(\Gamma_{qq'}) \vec{v}_q + H(-\Gamma_{qq'}) \vec{v}_{q'}], & \end{aligned}$$

$$\begin{aligned} \frac{\partial \bar{\rho}_M e_M}{\partial t} + \sum_{m \in M} \nabla \cdot (\bar{\rho}_M e_M \vec{v}_q) + P \left[\frac{\partial \alpha_M}{\partial t} + \nabla \cdot (\alpha_M \vec{v}_q) \right] & \\ - \frac{\bar{\rho}_M}{\bar{\rho}_q} \left[\sum_{q'} K_{qq'} (\vec{v}_q - \vec{v}_{q'}) (\vec{v}_q - \vec{v}_{qq'}) \right. & \\ \left. - K_{qs} \vec{v}_q \cdot (\vec{v}_q - \vec{v}_{qs}) - \overrightarrow{VM}_q \cdot (\vec{v}_{q'} - \vec{v}_{GL}) \right] & \\ = Q_{N,M} + Q_{MF,M} + Q_{VC,M} + Q_{HT,M}, & \end{aligned} \quad (1)$$

where subscripts m , q (or q'), and M denote the components of density, velocity, and energy, respectively; $\bar{\rho}$, α , \vec{v} , e , and Γ represent macroscopic (smeared) density, volume fraction, specific internal energy, and mass transfer rate, respectively; P , t , \vec{g} , and $H(x)$ are pressure, time, gravity, and Heaviside unit function, respectively; K_{qs} is momentum exchange function between q and structure; $\Gamma_{qq'}$ and $K_{qq'}$ are mass transfer rate and interfield momentum exchange function between q and q' , respectively; Q_{HT} , Q_{MF} , Q_N , and Q_{VC} are rates of energy interchange due to heat transfer, melting/freezing, nuclear heating rate, and vaporization/condensation, respectively; and, finally, \overrightarrow{VM}_q and $\overrightarrow{VM}_q \cdot (\vec{v}_{q'} - \vec{v}_{GL})$ are virtual mass terms in momentum and internal energy equations, respectively [19].

The overall fluid-dynamics solution algorithm is based on a time factorization approach originally developed for AFDM (advanced fluid-dynamics model) [19, 20], in which the intracell interfacial area source terms, heat and mass transfer, and momentum exchange functions are determined separately from intercell fluid convection. A semi-implicit procedure is used for the intercell convection. A higher-order differencing scheme is also implemented to improve the resolution of fluid interfaces by minimizing numerical diffusion.

In addition to the constitutive models, an equation-of-state (EOS) model is available to close and complete the fluid-dynamic conservation equations [19]. The analytic EOS model employs flexible thermodynamic functions that can be readily adapted to non-SFR materials based on experimental measurements.

2.2. Flow Regime and Interfacial Area Model. In the SIMMER-III calculation, the binary contact areas must be determined to obtain the mass, momentum, and energy transfer terms for the probable 52 contact interfaces among the 8 fluid energy components (liquid fuel, liquid steel, liquid sodium, fuel particle, steel particle, control particle, fuel chunks, and vapor mixture) and 3 structure surfaces (a fuel pin and left/right can walls) (see Figure 3) [19]. Such binary contact areas are determined based on the convective interfacial areas and a flow regime which describes the geometry of the multiphase flow.

In SIMMER-III, the multiple flow regimes are modeled for both pool flow, in which the effect of structure is

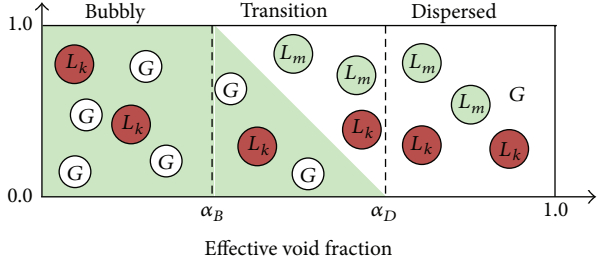


FIGURE 4: Pool flow regime map in SIMMER-III.

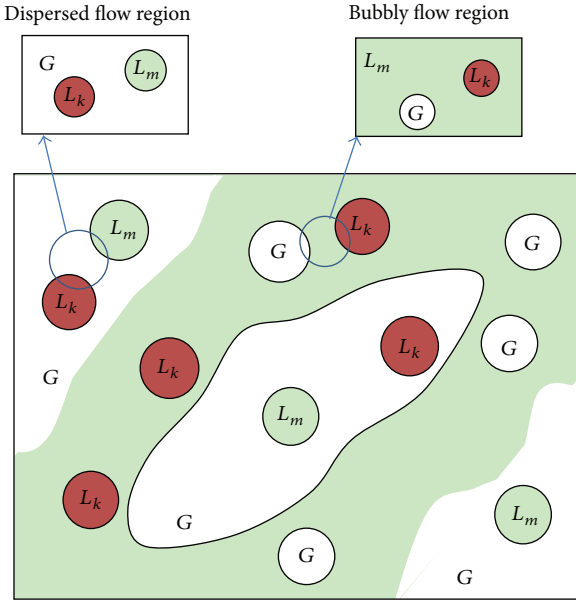


FIGURE 5: Schematic concept of separating bubbly and dispersed regions.

negligible, and channel flow, which is confined by structure [19]. As depicted in Figure 4, bubbly, dispersed, and in-between transition regimes are modeled for the pool flow which is the scenario involved in this study. The upper limit of the bubbly regime and the lower limit of the dispersed regime are defined by user-specified void fractions, α_B and α_D , respectively, with typical values being 0.3 and 0.7. In the SIMMER-III flow-regime modeling, it is generally assumed that a cell consists of two local regions, bubbly and dispersed regions as schematically described in Figure 5. The transition regime shown in Figure 4 is defined by a combination of the two regimes as a kind of interpolated flow regime. This treatment is advantageous because the flow characteristics can be determined continuously over the entire void fraction range, without abrupt change upon flow regime transition. To better represent the transient flow, SIMMER-III also has an interfacial area convection model, which is originally proposed by Ishii [19]:

$$\frac{\partial A_M}{\partial t} + \nabla \cdot (A_M \vec{v}) = \sum_k S_{M,k}, \quad (2)$$

where A_M is the interfacial area of component M and $S_{M,k}$ is the interfacial area source term (source k).

A total of nine interfacial areas associated to moving energy components are convected. These are the surface areas of real liquids (fuel, steel, and coolant) in the bubbly flow region; the surface areas of real liquids in the dispersed flow region; the surface areas of fuel and steel particles; and the surface area of bubbles in the bubbly flow region [19]. The changes of the interfacial areas due to processes of fragmentation, flashing, turbulence-driven breakup, coalescence, and droplet or bubble production are treated as “source terms” in the interfacial area convection equation [19]. The source term treatment in the interfacial area convection equation better represents the physical phenomena relevant to the change of interfacial areas. The modeling of the source terms is presently based on the AFDM approach except the droplet fragmentation [20]. The present SIMMER-III models only a hydrodynamically induced process as the fragmentation mechanism.

The source term of the hydrodynamic fragmentation is modeled by the following simple linear correlation assuming that the change of interfacial area S_d in time interval τ_d is equal to the average change of interfacial area:

$$S_d = \frac{A_d^e - A_d}{\tau_d}, \quad (3)$$

where the equilibrium interfacial area A_d^e is related through the equilibrium radius r_d^e and the volume fraction α_d of droplets:

$$A_d^e = \frac{3\alpha_d}{r_d^e}. \quad (4)$$

The equilibrium radius is assumed to be the maximum stable size of droplet governed by the hydrodynamic stability criterion related to a critical Weber number:

$$r_d^e = \frac{We_{Crt}\sigma}{2\rho_c\Delta v^2}, \quad (5)$$

where Δv is defined as an instantaneous relative velocity difference between continuous and dispersed phases and ρ_c is the continuous-phase density. A constant value of 12 is simply used for We_{Crt} , although strictly this is the value for suddenly induced relative velocity. Since (3) is used to calculate the source terms of the droplet fragmentation in the vapor continuous (dispersed flow) and liquid continuous (bubbly flow) regions, the surface tension of droplets σ in (5) is calculated by

$$\sigma = \sigma_d \quad (6a)$$

for the dispersed flow region and

$$\sigma = \sigma_d + \sigma_c - 2(\sigma_d\sigma_c)^{1/2} \quad (6b)$$

for the bubbly flow region, where σ_c and σ_d are the surface tension of the continuous and dispersed liquids, respectively, in contact with a third gas or vapor phase. Equation

(6b) is used to evaluate an interfacial tension between two immiscible liquid phases, although this relation is strictly appropriate to nonpolar materials [21]. The dimensional time scale t_b^* of the fragmentation process is often correlated with a dimensionless time of droplet breakup by Rayleigh-Taylor or Kelvin-Helmholtz instability:

$$t_b^* = \frac{\Delta \nu \varepsilon^{0.5}}{2r_d} \tau_d, \quad (7)$$

where ε is the density ratio of the continuous dispersed phases. Simpkins and Bales (1972) fitted gas-liquid data for complete droplet fragmentation of the Rayleigh-Taylor instability by the following functional form of the dimensionless time in terms of the instantaneous Bond number [22]:

$$t_b^* = 32.5 \text{Bo}^{-0.25}. \quad (8)$$

For liquid-liquid system, Yuen et al. (1994) correlated the dimensionless time based on the experimental data in the mercury/water system by [23]

$$t_b^* = 13.7 \text{Bo}^{-0.25}. \quad (9)$$

Although the coefficient in the above functional form may take different values depending on the definition of the end of the breakup process, these correlations predict that the breakup time in liquid-liquid systems is smaller than that in gas-liquid systems for the same Weber number if the Rayleigh-Taylor instability mechanism dominates the fragmentation process. In SIMMER-III, (8) and (9) are applied to the droplet fragmentation in the dispersed (vapor continuous) and bubbly (liquid continuous) flow regions, respectively. A similar approach using the different breakup times between liquid-liquid and gas-liquid systems was applied to the three-velocity field code IVA3, which solves particle-number-density equations instead of IFA convection equations [24].

2.3. Heat and Mass Transfer Model. In addition to the interfacial area, the heat transfer coefficients between fluids are required in heat and mass transfer calculations. In general, the definition of the coefficients corresponds to the heat transfer resistance between the bulk and the interface temperatures. For the convective heat transfer processes in droplets, the heat transfer coefficients are simply calculated by using thermal conductivity and heat transfer length assuming steady-state temperature profiles. The convective heat transfer in continuous fluids is modeled based on the Nusselt number empirical correlations.

After the interfacial areas and heat-transfer coefficients are obtained, the conservation equations without convection are solved for intracell heat and mass transfer in two steps [19]. The first step calculates the phase-transition processes occurring at interfaces, described by a nonequilibrium heat-transfer-limited model. This is a nonequilibrium process because the bulk temperature does not generally satisfy the phase-transition condition when the mass transfer occurs at the interface. The second step of mass and energy transfer

is through equilibrium process occurring when the bulk temperature satisfies the phase-transition condition.

The basic concept of the nonequilibrium mass transfer model is to determine phase-transition rate by energy balance at the interface between the energy components A and B as shown below. The heat transfer rates from the interface are

$$\begin{aligned} q_{A,B} &= a_{A,B} h_{A,B} (T_{A,B}^I - T_A) && \text{in component } A, \\ q_{B,A} &= a_{A,B} h_{B,A} (T_{A,B}^I - T_B) && \text{in component } B, \end{aligned} \quad (10)$$

where superscript I denotes the interface, T represents the temperature, and a and h are the interfacial area and heat transfer coefficient between components A and B , respectively.

The net energy transfer rate from the interface is defined as

$$q_{A,B}^I = q_{A,B} + q_{B,A}. \quad (11)$$

If the net heat flow, $q_{A,B}^I$, is zero, sensible heat is exchanged without phase transition. If $q_{A,B}^I$ is positive, the energy is lost at the interface, namely, either a liquid component freezes or a vapor component condenses. Then, the mass transfer rate for this case is determined from

$$\Gamma_{L,s}^I = \frac{q_{A,B}^I}{i_L - i_{\text{sol},s}} \quad (\text{if the liquid component freezes}) \quad (12)$$

or

$$\Gamma_{v,L}^I = \frac{q_{A,B}^I}{i_v - i_{\text{sat},L}} \quad (\text{if the vapor component condenses}), \quad (13)$$

where i is the specific enthalpy and subscripts L , s , and v are the components of liquid, solid, and vapor phase, respectively, while sat and sol represent saturation and solidus points, respectively.

If $q_{A,B}^I$ is negative, on the other hand, the energy is gained at the interface, namely, either a solid component melts or a liquid component vaporizes. Then, the mass transfer rate for this case is determined from

$$\Gamma_{s,L}^I = -\frac{q_{A,B}^I}{i_{\text{liq},L} - i_s} \quad (\text{if the solid component melts}) \quad (14)$$

or

$$\Gamma_{L,v}^I = -\frac{q_{A,B}^I}{i_{\text{sat},v} - i_L} \quad (\text{if the liquid component vaporizes}), \quad (15)$$

where subscript liq denotes the liquidus point.

In the above equations (12)~(15), the heat of phase transition (the effective latent heat) is defined as the difference between the enthalpy at the interface and the bulk enthalpy of a component undergoing the phase-transition process. Although more correctly the bulk enthalpy should be replaced by the interfacial one, SIMMER-III does not calculate temperature gradients in liquid and vapors.

TABLE 1: Measurement parameters and their descriptions.

| Parameters | Sensing location | Sensor description |
|-------------|--------------------|--------------------|
| Temperature | Melt | TM1~8 |
| | External wall | TW1~5 |
| | Cover gas | TG1~6 |
| | Water/flask | TF1~3 |
| Pressure | Melt | PS1~2 |
| | Cover gas | PT1~2 |
| Strain | Interaction vessel | SG1~2 |

3. SIMMER-III Application to Local FCI

To enhance the reliability of SIMMER-III code for reactor safety evaluation, in the past, a comprehensive and systematic assessment program of the code was conducted in two steps [7, 17, 19]: Phase 1, for fundamental assessment of individual code models, and Phase 2, for integral code assessment. Phase 1 assessment applied the code to single and multiphase flow benchmark problems, small-scale experiments with reactor and simulant materials, and physical problems with known solutions, while Phase 2 assessment involved applications of the code to integral and complex multiphase situations relevant to accident analyses, such as boiling and nonboiling pool dynamics [7, 17, 25], fuel relocation and freezing [26], fuel-coolant interaction [27, 28], core expansion dynamics, and disrupted core neutronics. The above two-step program was successfully conducted in collaboration with the European partners KIT (formerly known as FZK), CEA, and IRSN. It was demonstrated that the SIMMER-III code can reasonably simulate the highly transient multiphase phenomena occurring during CDAs [17, 27], even for the energetic FI-mode steam explosions [27]. Therefore, although further confirmation would be still necessary, to some degree, we do have some confidence for its utilization on the CI-mode FCIs, especially for the nonenergetic pure vapor generation and expansion events involved in this study.

3.1. Overview of Experiments. It is instructive to note that, over the past decades, extensive knowledge and findings on the CDAs have been accumulated, in response to the increase in experimental evidence and upgrading of computer codes [7]. For instance, it becomes gradually clear that the potential of forming a stable vapor film at the fuel-sodium interface during CDAs should not be quite high [29, 30]. Therefore, similar to the experimental study [16], here, our attention is solely confined on the nonfilm boiling conditions and the primary interest is to ascertain whether, under such a heat-exchange mode, a limited pressurization is maintainable, even if the water mass delivered into the pool is remarkably increased.

Figure 6 shows the representative experimental facility, while the relevant instrumentations are further described in Table 1. It can be seen that most of the apparatuses are contained in an outer vessel which provides protection from FCI events occurring in an interaction vessel located in it.

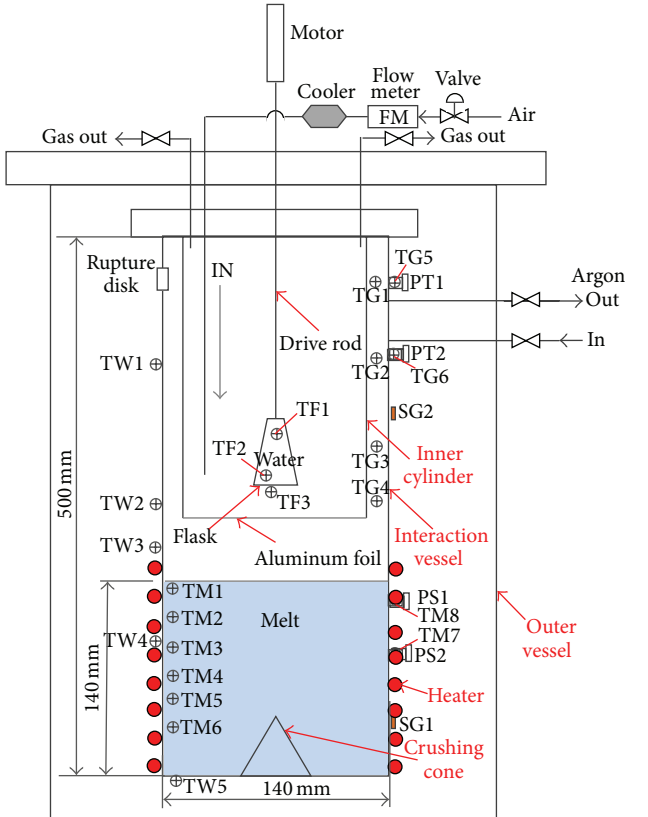


FIGURE 6: Representative experimental facility.

The interaction vessel is a rigid cylindrical stainless steel vessel of 140 mm in inner diameter. Several thermocouples, dynamic pressure transducers, and strain gauges are installed at different positions (see Figure 6). For all experimental runs, a low-melting-point alloy (Bi 60%-Sn 20%-In 20%), with its density and melting point being around 8500 kg/m^3 and 352 K, respectively, is utilized for simulating the fuel material. Before depositing on the bottom of the interaction vessel, the mass of the alloy blocks is well weighed so that the molten pool, formed later by heating the alloy blocks, can keep target heights.

Water is used as simulant material for coolant. The combination of water and the above-mentioned low-melting-point alloy has been elaborately selected after comprehensive

TABLE 2: Condition of experimental tests performed [16].

| Test number | Melt temperature (K) | Melt volume (cc) | Water temperature/subcooling (K) | Water volume (cc) |
|-------------|----------------------|------------------|----------------------------------|-------------------|
| 1 | 680 | | 331 (42) | 5 |
| 2 | 671 | | 331 (42) | 10 |
| 3 | 675 | | 330 (43) | 20 |
| 4 | 669 | 2154 | 330 (43) | 40 |
| 5 | 674 | | 331 (42) | 60 |
| 6 | 675 | | 331 (42) | 80 |
| 7 | 673 | | 331 (42) | 96 |

evaluation in cost, operation easiness, and feasibility of reliable measurement as well as the capability for simulating the potential local FCIs in accident conditions for SFRs from several aspects including melt density and density of liquid coolant and coolant vapor along with the typical nonfilm boiling heat-exchange modes [16, 29, 30]. Water, with its volume carefully measured, is loaded into a glass flask connected to the bottom end of the drive rod. Currently, different sizes of flask (such as 50 and 100 mL) can be utilized depending on the corresponding water volume required in an experimental run.

An electric heater, wrapped around the external wall of the interaction vessel, is used to heat the alloy and water. To avoid the heat convection within the interaction vessel (thereby ensuring the water temperature not to rise too rapidly), an inner cylinder, with its bottom covered by a thin aluminum foil, is equipped through hanging from the top of the interaction vessel. It should be recognized that the thin aluminum foil, despite being quite effective in preventing the heat convection between the melt and water regions, is susceptible to being pierced through by the drive rod, thereby leading to neglectable interference on the water-delivering process. During the heating, as illustrated in Figure 6, air and argon flows are being delivered, to achieve a more accurate control of water temperature and prevent the oxidation of the alloy, respectively.

After the temperature of water and melt reaches target values, through operating the motor, the flask is transported downwards and ruptured by a crushing cone prepositioned on the bottom of the interaction vessel. Before the initiation of any formal runs, several preliminary tests were performed to confirm that the flask can be thoroughly destroyed [16]. Therefore, the confining role of the flask, if any, is expected to be remarkably reduced during FCIs [16].

Table 2 lists the detailed condition of performed experimental tests [16]. Based on a film boiling criterion proposed from thermal aspect by Kondo et al. [29], it can be judged that the initial temperature of melt and water in those cases can guarantee that the nonfilm boiling mode should be attainable, although some uncertainties in hydrodynamic difference between the jet flow and current CI-mode condition might exist. In addition, from past SCARABEE tests [31], it becomes also known that, during the pool enlargement, coolant might be driven into the molten pool in a scenario where a comparatively larger pressure difference is produced by the

usual FCIs (i.e., the FI-mode) at the failure of control rod guide tube. Since, in such a scenario, the coolant subcooling may not decrease too much, therefore, as depicted in Table 2, relatively higher water subcooling (around 40 K) is employed for current tests.

3.2. Determination of Analytical Geometry and Condition. Prior to numerical calculation, it should be mentioned that, during experimental analyses [16], some experimental limitations and uncertainties have been recognized. Since some of those uncertainties, for example, the exact initial geometry of the water lump formed after the rupture of glass flask, might not be much easier to be modelled, therefore, for the calculation, a comparatively simplified scenario, which is achieved by eliminating the known experimental uncertainties as far as possible, is employed. We believe that, if the calculated results obtained from such a simpler idealized situation are basically consistent with the evidence that was confirmable by a much larger experimental database, it perhaps means that even if some uncertainties exist, the developed facility and method might be overall valid over current range of conditions.

Figure 7 illustrates the analytic geometry adopted. It is evident that, compared to the experimental facility (see Figure 6), a much larger dimension is applied. This treatment is specifically made due to the fact that, with the increasing water volume, the outer edge of water lump (i.e., the potential initial FCI sites) in the experiments might become closer to the pressure measuring points (e.g., the PS2), thereby leading to probably enlarged measurement errors. Further, we notice that although our developed experimental method (such as the water-delivery and subsequent flask-rupture process) provides an effective way to achieve well-controlled water mass as well as water and melt temperatures, it may also induce some pool fluctuations, as a result possibly impairing the accuracy of experimental analyses. To focus on the effect of water volume on local FCIs, a static water lump is assumed in our calculations.

Table 3 lists the conditions of the calculated runs in this work. To reduce the potential uncertainty caused by the initial geometry of water lump during experiments, an identical shape factor (i.e., radius/height = 1) is employed for the water column in all the runs calculated. To achieve such a shape factor more easily, as shown in Figure 7, a region of uniform fine meshes is applied within the interaction zone.

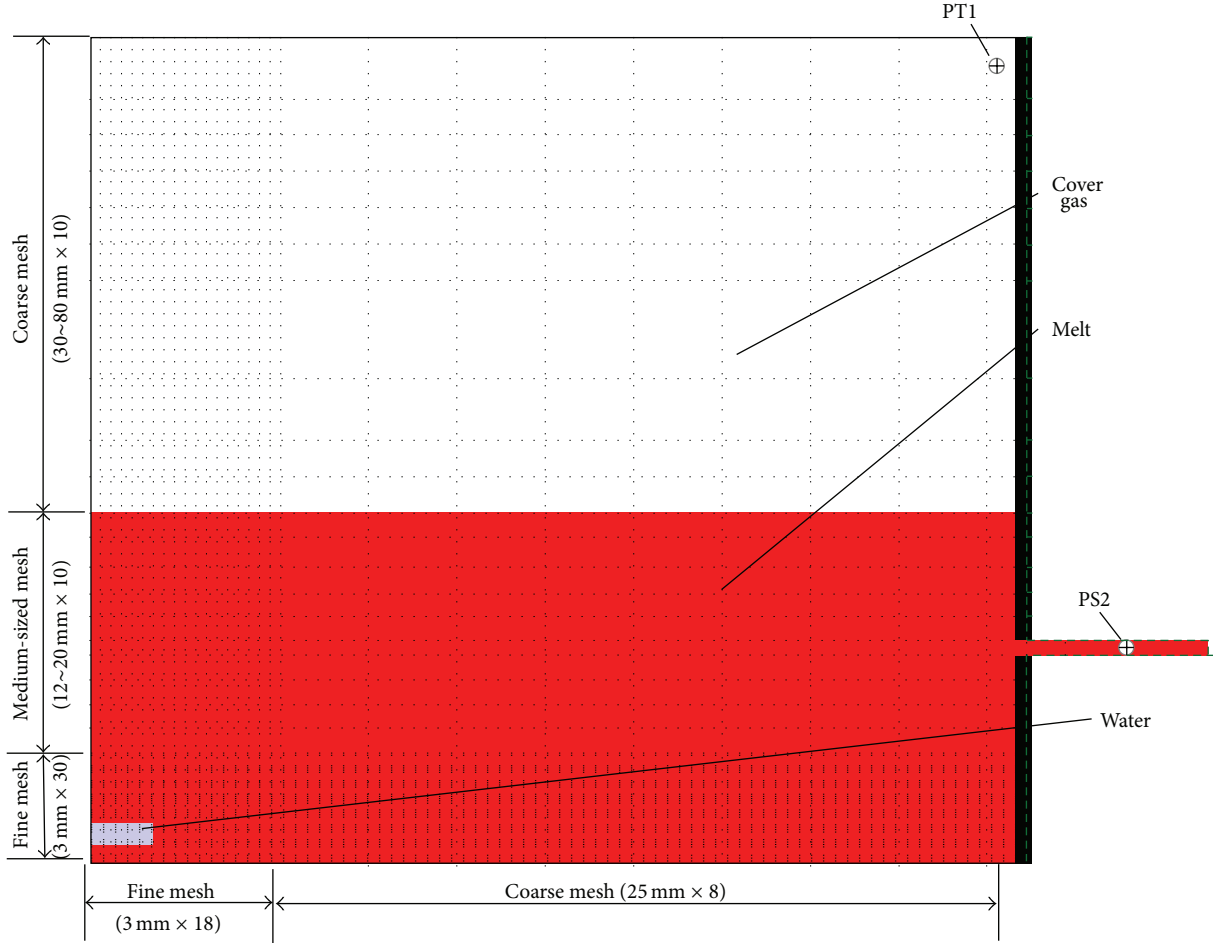


FIGURE 7: Analytical geometry.

TABLE 3: Conditions of calculated runs.

| Run number | Melt temperature (K) | Water temperature/subcooling (K) | Water volume (cc) |
|------------|----------------------|----------------------------------|--|
| 1-12 | 673 | 333 (40) | 0.7, 2.3, 5.4, 10.6, 18.3, 29.1, 43.4, 61.8, 84.8, 112.8, 146.5, and 186.3 |

4. Results of Analyses

Since a similar tendency of the pressure and temperature history can be observed for all the runs calculated in Section 4.1, a representative one, the Run #6, in which a volume of around 29.1 cc water is assumed to be entrapped within the melt pool, is randomly selected for illustrating the typical transient behavior predicted by SIMMER-III, while, in Sections 4.2 and 4.3, the interaction characteristics between different runs (e.g., pressure buildup, mechanical energy release, and its conversion efficiency) will be further examined and compared.

4.1. Transient Pressure and Temperature History in a Specific Case. Figure 8 shows the calculated temperature and pressure history for the Run #6, while Figure 9 further shows some representative visual frames. From the change of water temperature, it is evident that, after the water and melt are

directly contacted, a short premixing phase is observable. In addition, it can be also recognized that as compared to the melt temperature, the measured water temperature tends to be remarkably lower (<400 K), even after the completion of vapor expansion at around 0.06 s, which perhaps indicates that, for this case, only a limited quantity of liquid water is evaporated during the FCI occurrence. As for the melt part, possibly due to a greater dimension employed (resulting in much larger melt pool formed), different from experiments in which a noticeable decrease of melt temperature (around several tens of Kelvins) can be found [16], the average temperature of melt pool in the current simulation seems to be nearly constant, while, for the cover gas region, similar to experiments in [16], a quite rapid temperature increase (to be close to the melt temperature) exists. As pointed out in previous experimental analyses [16], in addition to the high-temperature steam generated, the rapid temperature increase for the cover gas should be also caused by the splashing of melt. In experimental analyses, this judgment is supportable

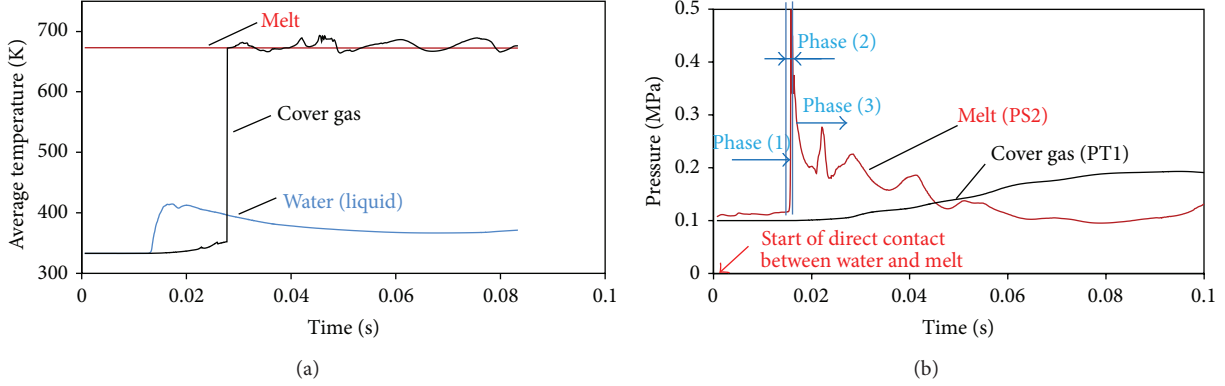


FIGURE 8: Temperature and pressure history for calculated Run #6.

by the posttest inspection that some solid alloy crusts can be found on the wall of the inner cylinder or/and the cover gas region of the interaction vessel, while, for the simulations, some visual evidence, for example, the ejection of melt (see Figure 9), is further observable.

From the melt pressure history shown in Figure 8, it seems that the pressure history, after the direct contact between melt and water is achieved, can be divided into three stages, namely, an initial mild change stage (or even constant for some specific runs), a rapid increase stage, and a decrease stage. By combining the visual observations from Figure 9, the following three-phase event progression might be identifiable: Phase (1), premixing of melt and coolant in which the vapor generation and condensation occurs simultaneously, Phase (2), rapid evaporation leading to short-term pressure buildup, and Phase (3), vapor expansion. In addition, similar to experimental results [16], it seems that the history of melt pressure can be also characterized by a two-phase pressure with its peak value and duration of less than 1.0 MPa and tens of milliseconds, respectively. As for the cover gas, possibly due to the significantly enlarged cover gas region (see Figures 6 and 7), a much mild pressure rising is observable as compared to previous experimental analyses [16].

4.2. Comparative Analyses of Pressure Buildup. Since, in actual reactor accident conditions, the compactive fluid motion is supposed to be triggered by a pressure pulse that pushes the liquid fuel away from the core center toward the core peripheries [4, 7], therefore, similar to previous experimental analyses [16], for the melt part, the impulse I on the melt slug, estimated by integrating the transient pressure P over time t and the cross-sectional area A_c of the interaction vessel, is used for the following analyses [16]:

$$I = A_c \int P(t) dt. \quad (16)$$

As for the cover gas region, the average pressure rising rate, defined as the ratio of the maximum pressure value to the time it needs to reach the maximum value, is used as well.

Figure 10 summarizes the pressure buildup characteristics for both the melt and cover gas regions as obtained from

SIMMER-III calculations and experimental measurements. It is evident that, although, possibly due to the remarkable difference encountered between experimental and calculated conditions (such as system dimension, melt mass, and height of melt pool as well as the volume of cover gas region), the absolute values are quite different, both the calculated and experimental results suggest that, with the increasing water volume, a limited pressurization is attainable during the local FCIs. In addition, it can be also found that, despite those differences, a knee point at a water volume of around 20 cc seems to be attainable for both calculations and experiments. Therefore, although further elaborated analyses might be preferable, to some extent, it is imaginable that possibly only a less part of melt (e.g., those close to the water lump) contributes to the rapid heat transfer during local FCIs.

Figure 11 shows the calculated steam generating rate from the time Phase (2) (see Figure 8) starts to the time the peak of the melt two-phase pressure is attained. It can be clearly seen that, as water volume increases, the steam generating rate seems to be increasing initially (<20 cc) and then tends to be saturated 20cc~(or >20cc), as a result suggesting the presence of a mechanism that suppresses the water evaporation.

It can be easily understood that a relatively larger volume (i.e., higher heat capacity) of water delivered into the pool (e.g., >20 cc) would probably lead the initial equilibrium temperature in the mixing region of the two fluids to be much decreased (through direct contact), as a result reducing the water evaporating rate and further restraining the followed pressure buildup. However, aside from this aspect, owing to the knowledge obtained from one of our past studies [7], in which the fuel-to-steel heat transfer characteristics were investigated within a molten fuel/steel mixture system, we believe that, although a stable film boiling contact mode should not appear within current melt and water temperature conditions, there is the possibility that the vapor bubbles generated at the interface to some extent may also hinder the direct contact between water and melt, leading to suppressed water evaporation. In addition, the remaining liquid water, before being driven away from its original site during the latter vapor expansion phase, might play a certain role as well in inhibiting the steam evaporation (e.g., through enhanced cooling or recondensation of the steam close to its

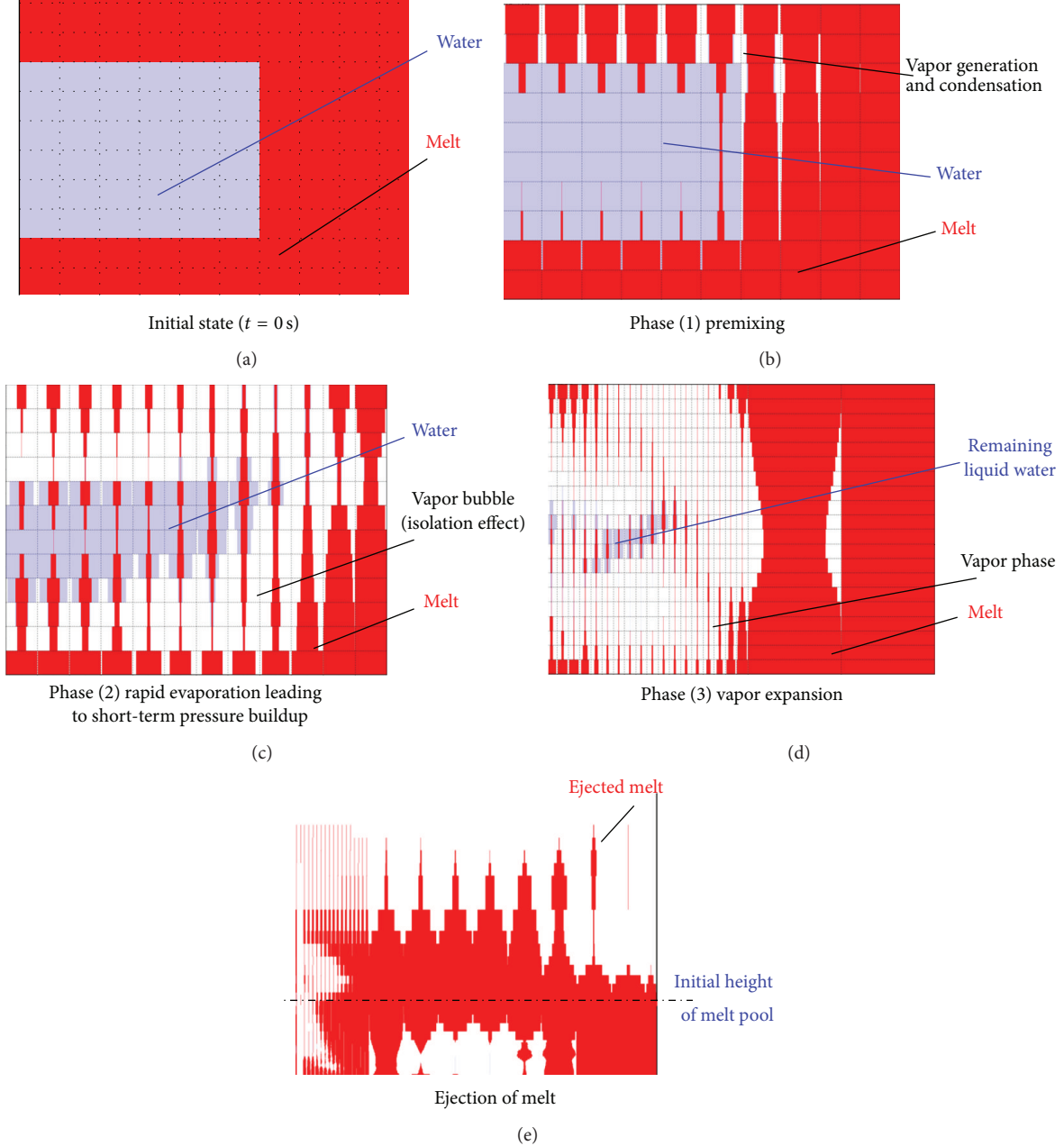


FIGURE 9: Material distribution in several representative frames for Run #6.

surface). However, we must notice that, physically speaking, the cooling effect caused by the remaining liquid water, should be only likely to act as a subordinate role, instead of the dominant one.

Table 4 lists the time period of the premixing phase as abstracted from SIMMER-III calculations for several cases within the saturated-pressure range. It can be easily seen that no evident variation is observable, even if the water volume entrapped within the pool is largely increased. Since, theoretically, such a time period should represent a kind of effective heat-transfer rate, to some extent, it might be deducible that the initial cooling of the surrounding melt by

the liquid water released should not play a remarkable role at current melt and water temperature conditions. In other words, although further confirmation would be inevitably necessary, we believe that the most probable reason leading to the limited pressurization in our study should be due to the isolation effect caused by the vapor bubbles generated at the melt-water interface, as might be qualitatively inferable as well from the visual evidence shown in Figure 9.

4.3. Comparative Analyses of Mechanical Energy Release. In general, total mechanical energy E_{TM} released in a FCI contains four parts [32], namely, the compression work of the

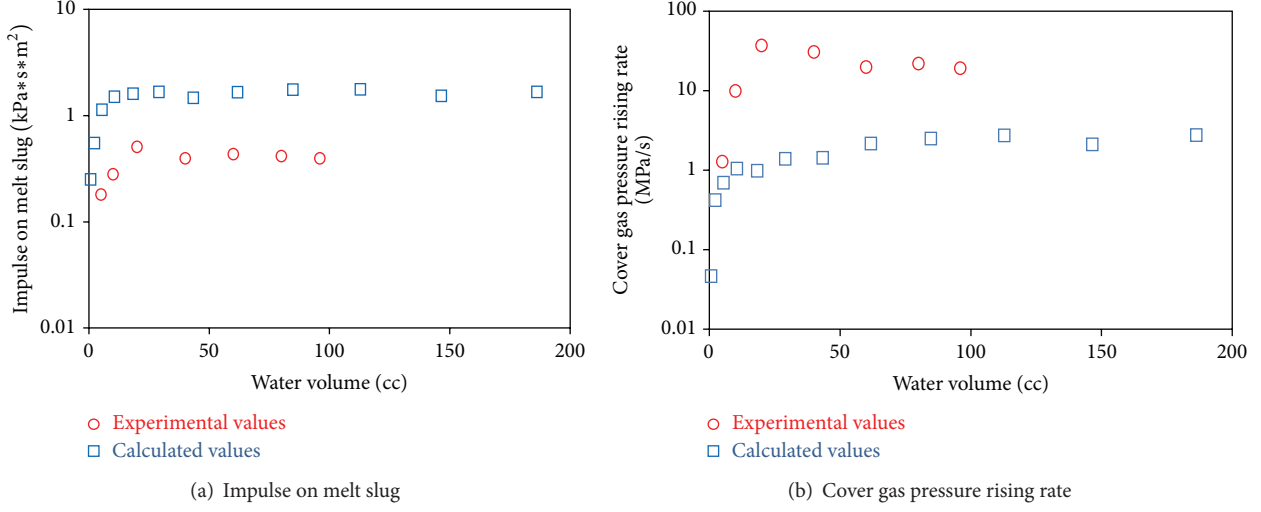


FIGURE 10: Experimental and calculated pressure characteristics at varying water quantities.

TABLE 4: Time period of premixing phase.

| | | | | | | | | |
|------------------------------------|-------|-------|-------|-------|-------|-------|-------|-------|
| Water volume [cc] | 18.3 | 29.1 | 43.4 | 61.8 | 84.8 | 112.8 | 146.5 | 186.3 |
| Time period of premixing phase [s] | 0.016 | 0.015 | 0.016 | 0.016 | 0.016 | 0.015 | 0.016 | 0.015 |

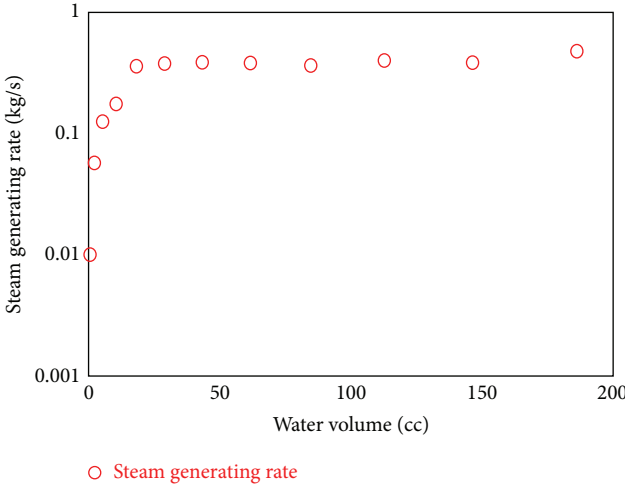


FIGURE 11: Calculated steam generating rate at varying water quantities.

cover gas (E_c), the kinetic energy (E_k) and potential energy (E_p) of the melt slug, and the strain energy of the interaction vessel wall (E_s). In our earlier experimental analyses [16], it has been confirmed that similar to the FI-mode investigations [32], E_c and E_k are the largest two contributions to the total released mechanical energy, while the fraction of E_p and E_s seems to be negligible (<5%). Therefore, in this study, E_{TM} will be simply approximated to

$$E_{\text{TM}} = E_c + E_k. \quad (17)$$

Since for all the experimental and calculated runs performed, the FCI events are observable to be completed within

an extremely short time (less than a scale of second) (see Figure 8), an adiabatic process is assumed for the calculation of E_c [27]:

$$\begin{aligned} E_c &= - \int_{V_0}^{V_1} P dV = - \int_{V_0}^{V_1} P_0 \left(\frac{V_0}{V} \right)^\gamma dV \\ &= \frac{P_0 V_0}{\gamma - 1} \left\{ \left(\frac{P_1}{P_0} \right)^{(\gamma-1)/\gamma} - 1 \right\}, \end{aligned} \quad (18)$$

where P_0 and P_1 are the initial and maximum pressures of the cover gas, respectively; V_0 , V_1 , and V are the volumes of cover gas corresponding to P_0 , P_1 , and P , respectively; and γ is the ratio of specific heats.

By assuming a one-dimensional acceleration of an inertial mass (melt slug), E_k can be estimated as [13, 32]

$$E_k = \frac{I^2}{2m_{\text{melt}}}, \quad (19)$$

where m_{melt} is the total melt mass.

Finally, the mechanical energy conversion efficiency η is defined as [32]

$$\eta = \frac{E_{\text{TM}}}{E_{\text{ther}}} = \frac{E_c + E_k}{E_{\text{ther}}}, \quad (20)$$

where E_{ther} is the total thermal energy used for the interaction. Although, in the past FI-mode investigations, it is more common to calculate E_{ther} from the exothermic (melt) side [12, 13, 32], in our earlier experimental study, regarding the CI-mode FCI [16], due to the unknown mass of melt involved in the interaction, based on energy conservation, the E'_{ther} ,

which is actually the maximum thermal energy absorbable by water, has been tentatively employed for analyses:

$$E'_{\text{ther}} = m_{\text{Twater}} \left(C_{\text{water}} \Delta T_{\text{sub}} + h_{lg} + C_{\text{steam}} (T_{\text{melt}} - T_{\text{sat}}) \right), \quad (21)$$

where m_{Twater} , C_{water} , ΔT_{sub} , and h_{lg} are the total mass, specific heat, subcooled degree, and vaporization heat of water, respectively, while C_{steam} and T_{sat} are the specific heat of the generated steam and the saturation temperature of water, respectively.

As for the numerical analyses, E_{ther} might be directly estimable from the melt side using the following form:

$$E_{\text{ther}} = C_{\text{melt}} \left(\sum_{i=1}^{i \text{ Max}} \sum_{j=1}^{j \text{ Max}} m_{i,j} T_{i,j} \Big|_{t=t_0} - \sum_{i=1}^{i \text{ Max}} \sum_{j=1}^{j \text{ Max}} m_{i,j} T_{i,j} \Big|_{t=t_F} \right), \quad (22)$$

where C_{melt} is the melt specific heat; $i \text{ Max}$ and $j \text{ Max}$ are the maximum number of meshes in radial (i) and axial (j) directions, respectively; and $m_{i,j}$ and $T_{i,j}$ are the mass and temperature of melt in mesh (i,j), respectively, while t_0 and t_F denote the initial and final time of local FCIs, respectively.

On the other hand, since the exact mass of steam generated is available from SIMMER-III calculations, E_{ther} might be approximated from the water side as well:

$$E_{\text{ther}} = m_{\text{Steam}} \left(C_{\text{water}} \Delta T_{\text{sub}} + h_{lg} + C_{\text{steam}} (T_{\text{melt}} - T_{\text{sat}}) \right), \quad (23)$$

where m_{Steam} is the mass of steam generated.

Figure 12 shows the calculated mechanical energy release based on (17)~(19). It can be clearly seen that both the experimental and SIMMER-III calculated data support that, as water volume increases, a saturated tendency of released mechanical energy is observable. Actually, it should not be surprising because the E_{TM} values are directly calculated based on the pressure data in both the melt and cover gas regions as shown in Figure 10. Another point that can be seen from Figure 12 is that, compared to the pressure characteristics, the difference in absolute values of E_{TM} seems to be less prominent. Again, it should be reasonable because, for a given mass of water, the released mechanical energy might be theoretically constant since, as aforementioned, only a less part of melt contributes to the rapid heat transfer during local FCIs, in spite of a much larger dimension employed in the SIMMER-III calculations as compared to the experimental facility.

Figure 13 shows the calculated total thermal energy E_{ther} based on the above three definitions ((21)~(23)). It is evident that, since only a limited part of water, as analyzed above, is probably evaporated during local FCIs, the conservative estimations based on (21), as employed in our earlier experimental analyses, would lead to rather overestimated E_{ther} values. In addition, the quite less difference between calculations using (22) and (23) seems to confirm our judgment in Section 4.2 that the cooling effect caused by the remaining liquid water should not be much notable.

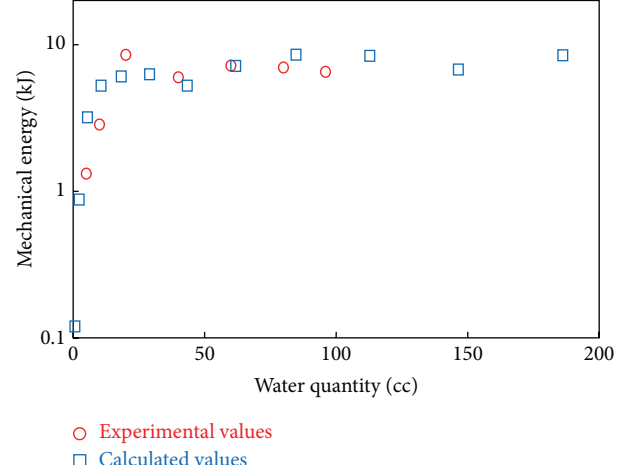


FIGURE 12: Experimental and calculated mechanical energy release at varying water quantities.

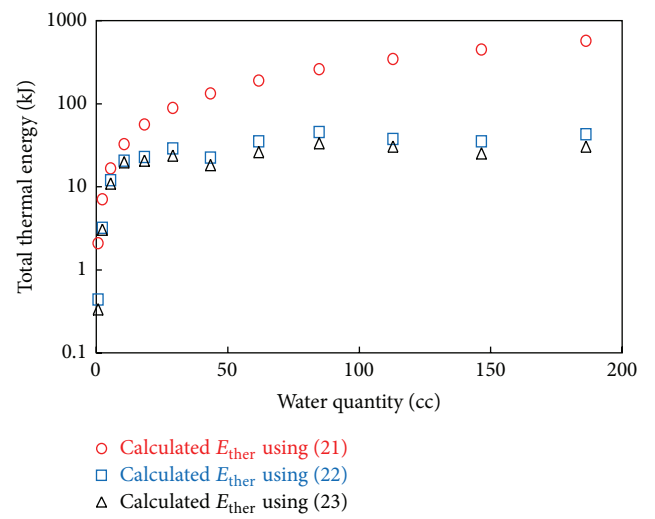


FIGURE 13: Estimated total thermal energy at varying water quantities.

Figure 14 illustrates the calculated conversion efficiency over varying water quantities. It can be easily seen that, as water volume increases, the calculated η seems to be slightly decreasing initially and then tends to be constant. This might be due to the fact that, at much lower water volume condition, the cooling effect caused by the remaining liquid water should be extremely lower or even negligible, as a result making the calculated η a little higher. On the other hand, for the calculations with much larger water volumes, the vapor bubbles generated at the melt-water interface, as mentioned above, to some extent may hinder the direct contact between melt and water, thereby resulting in saturated η values. Nevertheless, it seems that, for all the runs calculated, the obtained η values are varying over a comparatively narrow range (20~27%), which perhaps demonstrates again that the cooling effect induced by the remaining unevaporated water should be rather limited. Further, it is also confirmable that,

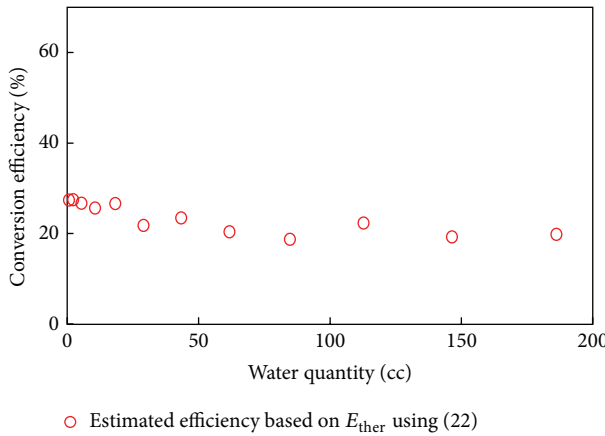


FIGURE 14: Estimated conversion efficiency at varying water quantities.

possibly due to the distinct difference involved in experimental conditions (e.g., material and temperature difference and interaction mechanism (steam explosion or nonsteam explosion) as well as interaction mode (FI or CI)), whatever the water volume is, the calculated η values are much higher than the reported results in several FI-mode investigations [12, 13, 32]. To further understand the difference between FI and CI modes, more calculations over a variety of parametric conditions are being planned.

5. Concluding Remarks

Motivated to provide further evidence for understanding the mechanisms of local FCIs in a molten pool, in this study, SIMMER-III, an advanced fast reactor safety analysis code, is used for analyses. Compared to experiments, the calculations were performed in a simpler idealized situation (namely, by lessening the known experimental uncertainties as far as possible). It is found that the SIMMER-III code can reasonably reflect the transient pressure and temperature tendencies during local FCIs as understood from experiments. In addition, from the comparative analyses between different cases, it is confirmable that, similar to experiments, as water volume increases, a limited pressure buildup and resultant mechanical energy release are observable. The good agreement on the evidence observed to some degree suggests that, despite the existence of some uncertainties, the developed experimental facility and method might be overall valid over current range of conditions, thereby providing us with enhanced confidence for future investigations using reactor material.

To estimate the mechanical energy conversion efficiency η , several definitions for estimating the total thermal energy E_{ther} are introduced. It is confirmable that the calculated η values in our experiments are much larger than the reported results in some FI-mode investigations.

Although a stable film boiling contact mode should not appear within current melt and water temperature conditions, the performed analyses in this work suggest that the

most probable reason leading to the limited pressurization and resultant mechanical energy release should be due to an isolation effect of steam bubbles generated at the melt-water interface.

Conflict of Interests

The authors declare that there is no conflict of interests regarding the publication of this paper.

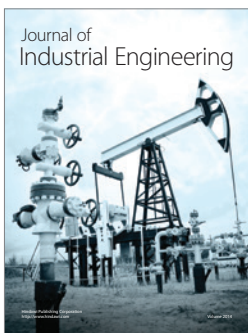
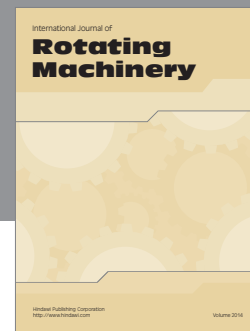
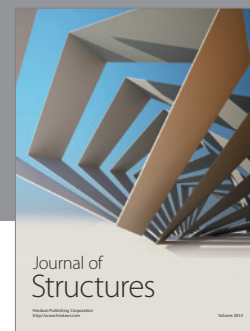
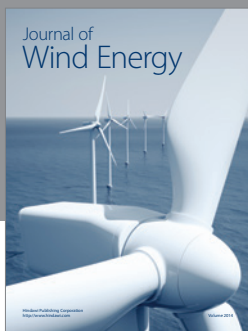
Acknowledgment

The authors would like to express their sincere gratitude to M. Sugaya of NESI Inc., for his technical assistance SIMMER-III running and analyses, which played an indispensable role in this study.

References

- [1] S. Cheng, H. Yamano, T. Suzuki et al., "Characteristics of self-leveling behavior of debris beds in a series of experiments," *Nuclear Engineering and Technology*, vol. 45, no. 3, pp. 323–334, 2013.
- [2] S. Cheng, H. Tagami, H. Yamano et al., "Evaluation of debris bed self-leveling behavior: a simple empirical approach and its validations," *Annals of Nuclear Energy*, vol. 63, pp. 188–198, 2014.
- [3] S. Cheng, H. Tagami, H. Yamano et al., "An investigation on debris bed self-leveling behavior with non-spherical particles," *Journal of Nuclear Science and Technology*, vol. 51, no. 9, pp. 1096–1106, 2014.
- [4] W. Maschek, C. Munz, and L. Meyer, "Investigations of sloshing fluid motions in pools related to recriticalities in liquid-metal fast breeder reactor core meltdown accidents," *Nuclear Technology*, vol. 98, no. 1, pp. 27–43, 1992.
- [5] T. G. Theofanous and C. R. Bell, "An assessment of clinch river breeder reactor core disruptive accident energetics," *Nuclear Science and Engineering*, vol. 93, no. 3, pp. 215–228, 1986.
- [6] Y. Tobita, K. Morita, K. Kawada, H. Niwa, and N. Nonaka, "Evaluation of CDA energetics in the prototype LMFBR with latest knowledge and tools," in *Proceedings of the 7th International Conference on Nuclear Engineering (ICONE' 99)*, Tokyo, Japan, April 1999.
- [7] H. Yamano, Y.-I. Onoda, Y. Tobita, and I. Sato, "Transient heat transfer characteristics between molten fuel and steel with steel boiling in the CABRI-TPA2 test," *Nuclear Technology*, vol. 165, no. 2, pp. 145–165, 2009.
- [8] T. Suzuki, K. Kamiyama, H. Yamano et al., "Evaluation of core disruptive accident for sodium-cooled fast reactors to achieve in-vessel retention," in *Proceedings of the 8th Japan-Korea Symposium on Nuclear Thermal Hydraulics and Safety (NTHAS '12)*, Beppu, Japan, December 2012.
- [9] T. Suzuki, K. Kamiyama, H. Yamano et al., "A scenario of core disruptive accident for Japan sodium-cooled fast reactor to achieve in-vessel retention," *Journal of Nuclear Science and Technology*, vol. 51, no. 4, pp. 493–513, 2014.
- [10] B. W. Spencer, K. Wang, C. A. Blomquist, L. M. Mcumber, and J. P. Schneider, "Fragmentation and quench behavior of corium melt streams in water," Tech. Rep. NUREG/CR-6133, ANL-93/32, Argonne National Laboratory, Lemont, Ill, USA, 1994.

- [11] I. Huhtiniemi, D. Magallon, and H. Hohmann, "Results of recent KROTOS FCI tests: alumina versus corium melts," *Nuclear Engineering and Design*, vol. 189, no. 1, pp. 379–389, 1999.
- [12] D. Magallon, "Characteristics of corium debris bed generated in large-scale fuel-coolant interaction experiments," *Nuclear Engineering and Design*, vol. 236, no. 19–21, pp. 1998–2009, 2006.
- [13] J. H. Kim, B. T. Min, I. K. Park, and S. W. Hong, "Triggered steam explosions with the corium melts of various compositions in a two-dimensional interaction vessel in the troi facility," *Nuclear Technology*, vol. 176, no. 3, pp. 372–386, 2011.
- [14] H. S. Park, N. Yamano, Y. Maruyama, K. Moriyama, Y. Yang, and J. Sugimoto, "Study on energetic fuel-coolant interaction in the coolant injection mode of contact," in *Proceedings of the 6th International Conference on Nuclear Engineering (ICON' 98)*, San Diego, Calif, USA, May 1998.
- [15] Y. Sibamoto, Y. Kukita, and H. Nakamura, "Visualization and measurement of subcooled water jet injection into high-temperature melt by using high-frame-rate neutron radiography," *Nuclear Technology*, vol. 139, no. 3, pp. 205–220, 2002.
- [16] S. Cheng, K. Matsuba, M. Isozaki, K. Kamiyama, T. Suzuki, and Y. Tobita, "The effect of coolant quantity on local fuel-coolant interactions in a molten pool," *Annals of Nuclear Energy*, vol. 75, no. 1, pp. 20–25, 2015.
- [17] Y. Tobita, S. Kondo, H. Yamano et al., "The development of SIMMER-III, an advanced computer program for LMFR safety analysis, and its application to sodium experiments," *Nuclear Technology*, vol. 153, no. 3, pp. 245–255, 2006.
- [18] K. Kamiyama, Y. Tobita, T. Suzuki, and K. Matsuba, "Development of an evaluation methodology for the fuel-relocation into the coolant plenum in the core disruptive accident of sodium-cooled fast reactors," in *Proceedings of the 22nd International Conference on Nuclear Engineering (ICON' 22)*, vol. 3, p. 12, Prague, Czech, July 2014.
- [19] H. Yamano, S. Fujita, Y. Tobita et al., *SIMMER-III: A Computer Program for LMFR Core Disruptive Accident Analysis, Version 3. A Model Summary and Program Description*, Japan Nuclear Cycle Development Institute, 2003.
- [20] W. R. Bohl, D. Wilhelm, F. R. Parker, J. Berthier, L. Goutagny, and H. Ninokata, "AFDM: an advanced fluid dynamics model, vol. I: scope, approach and summary," Los Alamos National Laboratory LA-11692-MS, 1990.
- [21] V. P. Carey, *Liquid-Vapor Phase-Change Phenomena: An Introduction to the Thermophysics of Vaporization and Condensation Processes in Heat Transfer Equipment*, Hemisphere, Washington, DC, USA, 1992.
- [22] P. G. Simpkins and E. L. Bales, "Water-drop response to sudden accelerations," *Journal of Fluid Mechanics*, vol. 55, no. 4, pp. 629–639, 1972.
- [23] W. W. Yuen, X. Chen, and T. G. Theofanous, "On the fundamental microinteractions that support the propagation of steam explosions," *Nuclear Engineering and Design*, vol. 146, no. 1–3, pp. 133–146, 1994.
- [24] H. Jacobs, "Analysis of large-scale melt-water mixing events," in *Proceedings of the CSNI Specialists Meeting on Fuel-Coolant Interactions*, Santa Barbara, Calif, USA, January 1993.
- [25] P. Liu, S. Yasunaka, T. Matsumoto et al., "Dynamic behavior of a solid particle bed in a liquid pool: SIMMER-III code verification," *Nuclear Engineering and Design*, vol. 237, no. 5, pp. 524–535, 2007.
- [26] K. Kamiyama, D. J. Brear, Y. Tobita, and S. Kondo, "Establishment of freezing model for reactor safety analysis," *Journal of Nuclear Science and Technology*, vol. 43, no. 10, pp. 1206–1217, 2006.
- [27] K. Morita, S. Kondo, Y. Tobita, and D. J. Brear, "SIMMER-III applications to fuel-coolant interactions," *Nuclear Engineering and Design*, vol. 189, no. 1–3, pp. 337–357, 1999.
- [28] X. Cao, Y. Tobita, and S. Kondo, "A thermal fragmentation model induced by surface solidification," *Journal of Nuclear Science and Technology*, vol. 39, no. 6, pp. 628–636, 2002.
- [29] S. Kondo, K. Konishi, M. Isozaki, S. Imahori, A. Furutani, and D. J. Brear, "Experimental study on simulated molten jet-coolant interactions," *Nuclear Engineering and Design*, vol. 155, no. 1–2, pp. 73–84, 1995.
- [30] K. Kamiyama, M. Saito, K.-I. Matsuba et al., "Experimental study on fuel-discharge behaviour through in-core coolant channels," *Journal of Nuclear Science and Technology*, vol. 50, no. 6, pp. 629–644, 2013.
- [31] G. Kayser, J. Charpenel, and C. Jamond, "Summary of the SCARABEE-N subassembly melting and propagation tests with an application to a hypothetical total instantaneous blockage in a reactor," *Nuclear Science and Engineering*, vol. 128, no. 2, pp. 144–185, 1998.
- [32] T. Tsuruta, M.-A. Ochiai, and S. Saito, "Fuel fragmentation and mechanical energy conversion ratio at rapid deposition of high energy in LWR fuels," *Journal of Nuclear Science and Technology*, vol. 22, no. 9, pp. 742–754, 1985.



Hindawi

Submit your manuscripts at
<http://www.hindawi.com>

